

Article

# Feasibility of Wave Simulation in Typhoon Using WAVEWATCH-III Forced by Remote-Sensed Wind

Ru Yao <sup>1</sup>, Weizeng Shao <sup>1,2,\*</sup>, Youguang Zhang <sup>3</sup>, Meng Wei <sup>1</sup>, Song Hu <sup>1</sup> and Juncheng Zuo <sup>1</sup>

<sup>1</sup> College of Marine Sciences, Shanghai Ocean University, Shanghai 201306, China; m210200552@st.shou.edu.cn (R.Y.); m220200613@st.shou.edu.cn (M.W.); shu@shou.edu.cn (S.H.); jczuo@shou.edu.cn (J.Z.)

<sup>2</sup> Key Laboratory of Space Ocean Remote Sensing and Application, Ministry of Natural Resources, Beijing 100081, China

<sup>3</sup> National Satellite Ocean Application Service, Ministry of Natural Resources, Beijing 100081, China; zhanyouguang@mail.nsoas.org.cn

\* Correspondence: wzshao@shou.edu.cn; Tel.: +86-21-61900326

**Abstract:** The purpose of our work was to assess the feasibility of hindcasting waves using WAVEWATCH-III (WW3) in a typhoon by assembling winds from multiple remote-sensed products. During the typhoon season in 2021–2022, the swath wind products in the Western Pacific Ocean were collected from scatterometers and radiometers. Cyclonic winds with a spatial resolution of 0.125° at intervals of 6 h were obtained by assembling the remote-sensed winds from those satellites. The maximum wind speeds,  $V_{max}$ , were verified using the reanalysis data from the National Hurricane Center (NHC), yielding a root-mean-squared error (RMSE) of 4.79 m/s and a scatter index (SI) value of 0.2. The simulated wave spectrum was compared with the measurements from Surface Waves Investigation and Monitoring (SWIM) carried out on the Chinese–French Oceanography Satellite (CFOSAT), yielding a correlation coefficient (Cor) of 0.80, squared error (Err) of 0.49, RMSE of significant wave height (SWH) of 0.48 m with an SI of 0.25, and an RMSE of the peak wave period (PWP) of 0.95 s with an SI of 0.10. The bias of wave (WW3 minus European Centre for Medium-Range Weather Forecasts (ECMWFs) reanalysis (ERA-5)) concerning the bias of wind (assembling minus ERA-5) showed that the WW3-simulated SWH with the assembling wind forcing was significantly higher than that with the ERA-5 wind forcing. Moreover, the bias of SWH gradually increased with an increasing bias of wind speed; i.e., the bias of SWH increased up to 4 m as the bias of wind speed reached 30 m/s. It was concluded that the assembling wind from multiple scatterometers and radiometers is a promising source for wave simulations via WW3 in typhoons.

**Keywords:** wave; WAVEWATCH-III; assembling wind



**Citation:** Yao, R.; Shao, W.; Zhang, Y.; Wei, M.; Hu, S.; Zuo, J. Feasibility of Wave Simulation in Typhoon Using WAVEWATCH-III Forced by Remote-Sensed Wind. *J. Mar. Sci. Eng.* **2023**, *11*, 2010. <https://doi.org/10.3390/jmse11102010>

Academic Editor: João Miguel Dias

Received: 28 August 2023

Revised: 7 October 2023

Accepted: 13 October 2023

Published: 19 October 2023



**Copyright:** © 2023 by the authors. Licensee MDPI, Basel, Switzerland. This article is an open access article distributed under the terms and conditions of the Creative Commons Attribution (CC BY) license (<https://creativecommons.org/licenses/by/4.0/>).

## 1. Introduction

Typhoons frequently occur in the Western Pacific Ocean [1] and play an essential role in the momentum and heat exchange. Observations from moored buoys and remote-sensing equipment, i.e., an altimeter [2] and a wave spectrometer (Surface Waves Investigation and Monitoring (SWIM)) based on the Chinese–French Oceanography Satellite (CFOSAT) [3], are valuable sources of data for research on typhoon-induced waves. However, high-precision on-site observations lack continuity on temporal and spatial scales. Moreover, measurements from the abovementioned remote-sensed techniques, which release data with a 1–2-day delay, have coarse spatial resolution, i.e., 10 km for the altimeter and 18 km for SWIM. Moreover, sea surface wind and waves can be simultaneously inverted from synthetic aperture radar (SAR) images, i.e., up to a 1 m pixel size for X-band TerraSAR-X [4] and C-band Gaofen-3 [5]. As an increasing number of satellites are launched, it is vital to cooperatively apply these advanced techniques in oceanic dynamics monitoring, such as in the study of strong-wind-induced waves during typhoons.

The sea surface wind field is an essential aspect of typhoon-associated hazard [6], which also determines the drag coefficient and also generates waves [7,8]. Operational products from atmospheric prediction systems [9,10], i.e., the European Centre for Medium-Range Weather Forecasts (ECMWFs) and the National Centers for Environmental Prediction (NCEP) Global Forecast System (GFS), are usually used as the forcing field in wave hindcasting based on numeric models. However, as revealed in [11], the wind fields from numerical weather prediction systems have significant distortions during typhoons. Hence, wave simulations using these wind products as the forcing field lead to inaccurate forecasting and hindcasting products. Since the 1980s, satellite remote sensing technology has rapidly developed, and operational products can be released daily. Nowadays, scatterometers and radiometers are effective instruments for wind monitoring over the global ocean. The detectable maximum wind speeds from the scatterometer are only up to 25 m/s [12], whereas the radiometer does not suffer this problem. However, the spatial resolution of the scatterometer can reach 12.5 km over the swath with approximately 100 km, which is higher than a typical 0.25° grid of the radiometer. Although remote-sensed winds are available in descending and ascending directions, the temporary resolution is anticipated to be improved using multiple satellites.

Numerical models are widely used methods for hindcasting and predicting sea surface waves over global [13] and regional [14] oceans. Third-generation numerical models, i.e., WAVEWATCH-III (WW3) [15,16] and Simulation Wave Nearshore (SWAN) [17], are popular for wave hindcasting, with fine spatial resolutions and wide coverage, especially in typhoons [18]. The main difference between the two numerical models is the computational grid, i.e., the rectangle grid for WW3 [19–21] and the unstructured grid for SWAN [22]. However, the newly updated versions of these models can employ both rectangle and unstructured grids. The acquisition of precise cyclonic wind data in typhoons is still a challenge, which restricts the accuracy of wave simulations via numerical models due to the strong heat and momentum exchange at the air-sea interface. Although in situ observations from moored buoys are assimilated in a reanalysis system such as ECMWFs, the underestimation of wind speeds needs to be reduced in tropical cyclones (TCs) based on the parametric wind profile model [23]. This leads to the difficulty of wave simulation using numeric models under extreme weather conditions. This difficulty could be solved using real measurements from remote-sensed wind products. Although assembling winds from remote-sensed products has served as the forcing field for the numeric wave model over the global ocean [24], the feasibility and accuracy of remote-sensed wind data used in typhoon-induced wave simulation are important questions worth investigating. At present, typhoon-induced waves are usually simulated via the wave model forced by reconstructed wind products [25] and predicted via artificial intelligence methods with remote-sensed products [26]. The application of assembling winds from remote-sensed winds in a typhoon-induced wave simulation has not been examined. An experiment utilizing multiple satellites is carried out in this study to explore this issue.

In this study, the simulated region is located in the Western Pacific Ocean with a wide spatial coverage, indicating that the rectangular grid used in WW3 has better computational efficiency than the unstructured grid in SWAN. This study aims to assess the feasibility and accuracy of assembling winds from remote-sensed wind data used in the typhoon-induced wave simulation via the WW3 model. Section 2 shows the data collection from typhoons, including operational wind products from nine scatterometers and radiometers, including the Advanced Scatterometer (ASCAT-A/B/C) and Haiyang-2 (HY-2B/C/D) constellation. The radiometers consist of Soil Moisture Active–Passive (SMAP), Advanced Microwave Scanning Radiometer-2 (AMSR-2) and HY-2B, and wave spectra from SWIM. The methodology for assembling wind and the metric parameters is also presented in Section 2. Section 3 provides the verification of WW3-simulated waves using the assembling wind forcing field and ERA-5 wind forcing field, respectively, against the measurements of SWIM and provides further discussion. Finally, the conclusion is given in Section 4.

## 2. Data and Method

In this section, the wind measurements from multiple satellites and the approach for assembling winds from multiple satellites are described. A description and settings of WW3 are introduced. Additionally, ECMWFs reanalysis (ERA-5) of winds, waves, and altimeter-measured significant wave heights (SWHs) are presented. Lastly, the metric variables for the error analysis are shown.

### 2.1. Remote-Sensed Products and Assembling Method

During the typhoon season in 2021–2022, scatterometer and radiometer wind products were acquired in the Western Pacific Ocean. Figure 1 shows the tracks and maximum wind speeds  $V_{max}$  in 30 typhoons during the 2021–2022 typhoon season from the National Hurricane Center (NHC). The area marked by the black rectangle is the modeling region ( $100^\circ$  E– $180^\circ$  E,  $0^\circ$  N– $60^\circ$  N). Some scatterometer and radiometer wind products were acquired for the Western Pacific Ocean region in this period. In this study, the scatterometers include ASCAT-A/B/C and HY-2B/C/D constellations. The radiometers consist of Soil Moisture Active–Passive (SMAP), Advanced Microwave Scanning Radiometer-2 (AMSR-2), and HY-2B. It is necessary to clarify that wind direction data are not available from the radiometer. These products were calibrated and are useful for the study of atmosphere and oceanography in tropical cyclones [27,28]. The wind vectors measured from the HY-2B scatterometer and radiometer [29] on 26 September 2021 are presented in Figure 2a and Figure 2b, respectively.

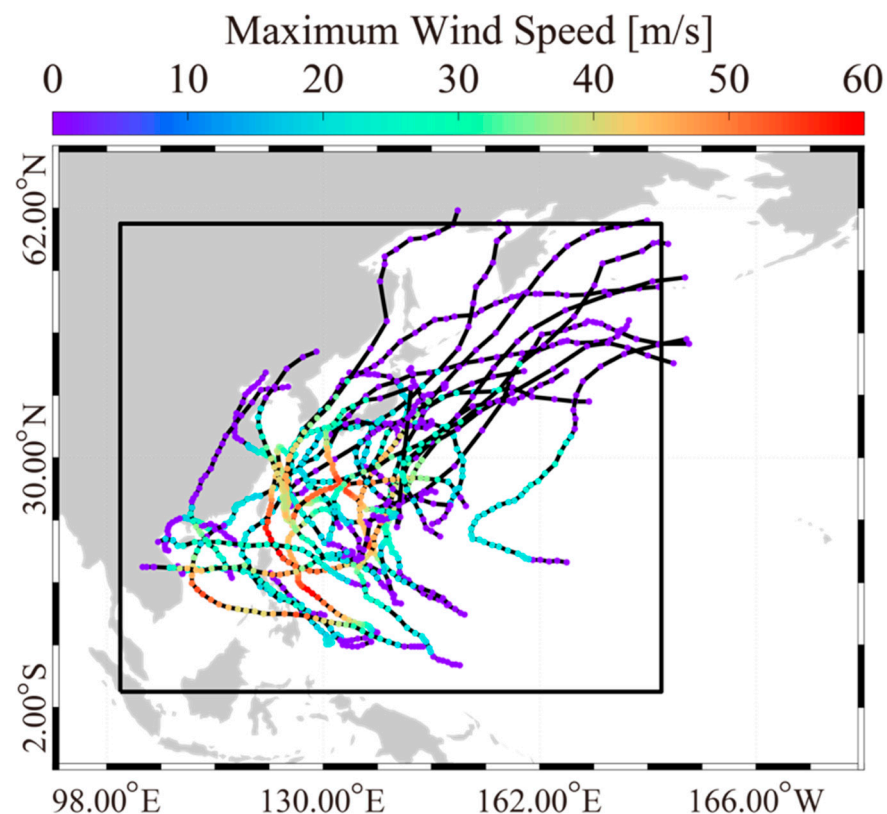


**Figure 1.** Information on typhoons obtained from the National Hurricane Center (NHC), in which the black rectangle represents the modeling region and the color lines correspond the best tracks of typhoons.

At present, the wave spectrum can be inferred from SAR [30] and SWIM, especially in tropical cyclones [31,32]. Unfortunately, the accuracy of wave retrieval from typhoon SAR images necessitates further improvements [33], and there are few SAR images of the above typhoons. Here, the SWIM-measured wave spectra of 30 typhoons are used for

validating the simulations from WW3. Note that the SWIM-measured wave spectrum has  $180^\circ$  ambiguity; therefore, a comparison of the wave directions between SWIM and WW3 is not conducted in our work. Moreover, the SWIM-measured wave spectrum is transformed to the wave number space and then compared with WW3 simulations.

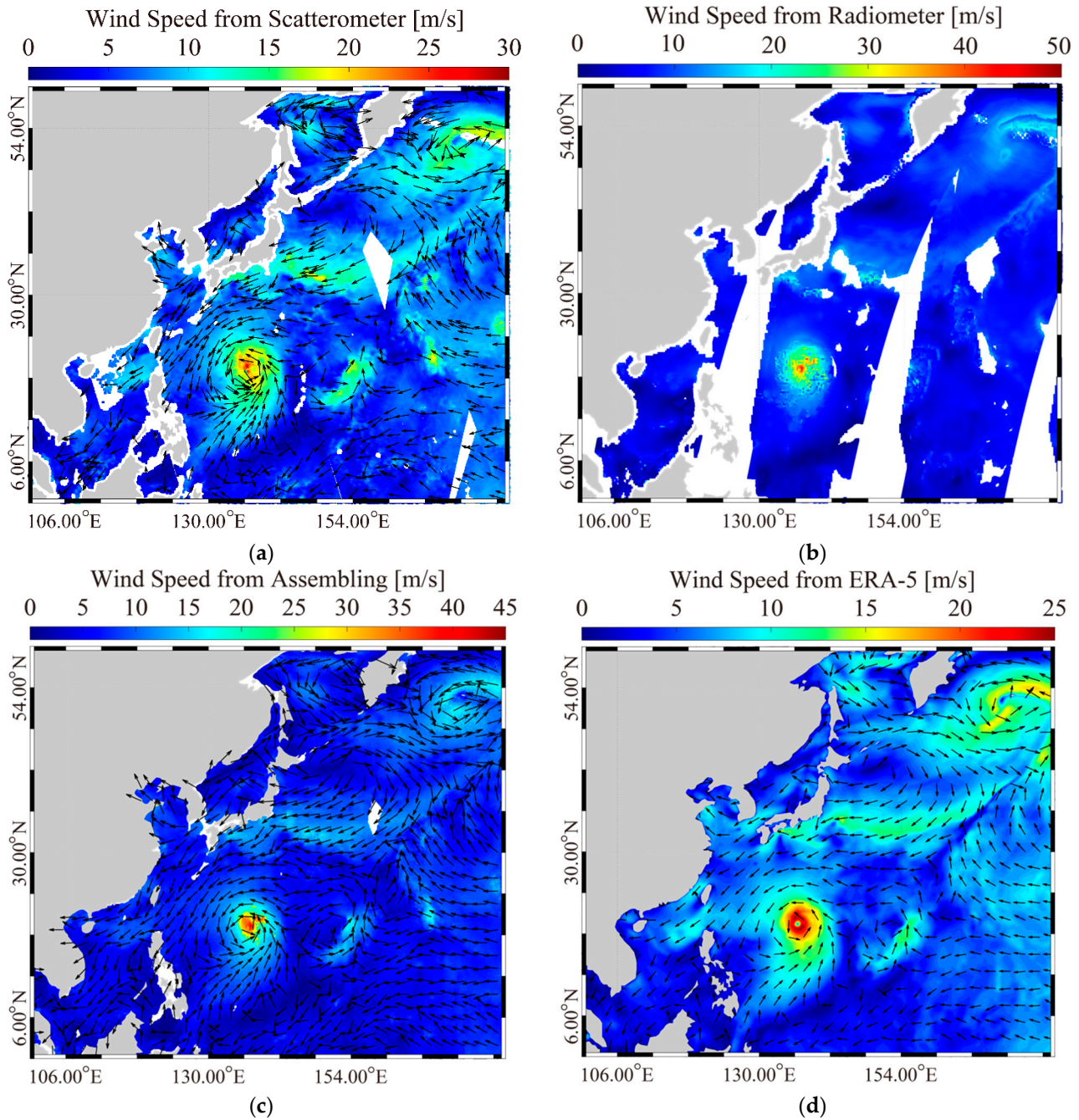
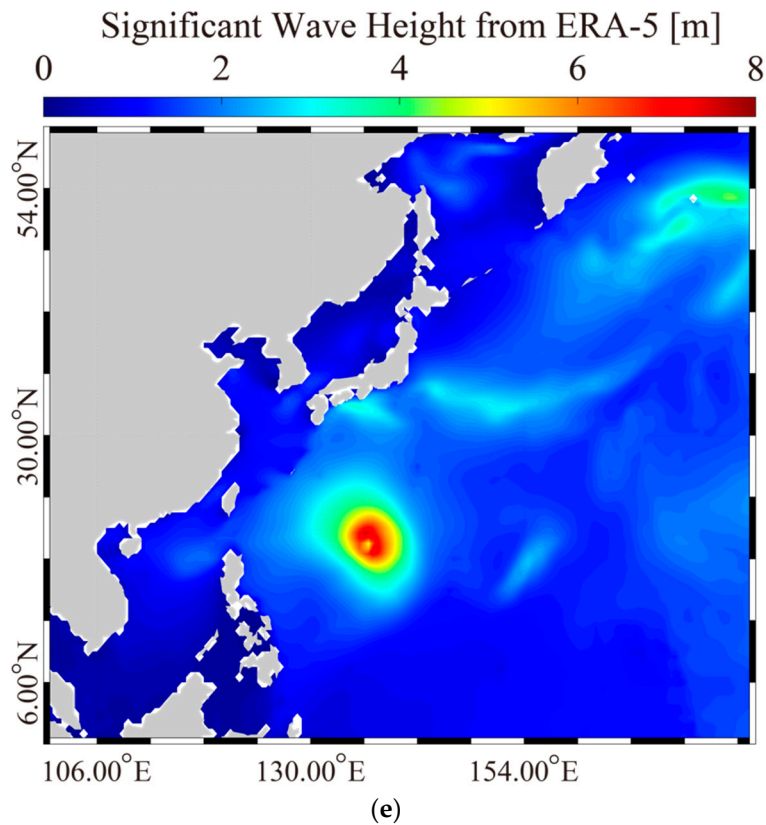


Figure 2. Cont.



**Figure 2.** Wind maps from (a) Haiyang-2B (HY-2B) scatterometer and (b) radiometer. (c) The wind map from assembling data during Typhoon Mindulle at 18:00 UTC on 26 September 2021. European Centre for Medium-Range Weather Forecasts (ECMWFs) reanalysis (ERA-5) maps during Typhoon Mindulle at 18:00 UTC on 26 September 2021: (d) wind and (e) significant wave height (SWH).

In 1978, SEASAT carrying an altimeter demonstrated the feasibility of SWH measurements when using an altimeter. From then on, spaceborne radar altimeters have been rapidly developed worldwide, e.g., the Jason-2/3 working with the Ocean Surface Topography Mission (OSTM) and the HY-2 satellite constellation. The footprint-following altimeter-measured SWHs have a spatial coverage of 10 km with highly detailed data of the sea surface. The cooperative satellite Jason-3, launched in 2016 by international agencies (NOAA, CNES, and EUMETSAT), provides well-calibrated wave products such as SWHs. In this study, the monthly averaged SWHs from Jason-3 altimeter products from January 2021 to December 2022 were used for conducting the error analysis of the wave simulations from the WW3 model.

The Cressman interpolation method based on the distance is used for assembling remote-sensed winds, which is expressed as

$$\vec{u}_f = \vec{u}_0 + \frac{1}{n} \sum_{i=1}^n W_i \Delta \vec{u}_i \tag{1}$$

where  $\vec{u}_0$  is the wind velocity vector from the initial HY-2B scatterometer (<25 m/s) or radiometer ( $\geq 25$  m/s) nearest to the assembling point;  $n$  represents the numbers of available wind vectors within the spatial resolution of assembling wind ( $R$ ) assumed to be a  $0.125^\circ$  grid;  $\Delta \vec{u}_i$  is the difference between individual referred wind and the initial wind vector; and  $W_i$  is the distance-dependant weight, stated as

$$W_i = \frac{D_i^2 - R^2}{D_i^2 + R^2} \tag{2}$$

in which  $D_i$  is the distance between the individual referred wind and the initial wind vector. The temporal resolution of the assembling wind is 6 h. The above interpolation has been used for SAR wind retrieval in previous studies [4] because the spatial resolution of interpolation can be selected artificially. Note that the wind direction is directly obtained from a scatterometer because the radiometer provides no wind direction. Figure 2c shows the assembling wind map during Typhoon Mindulle at 18:00 UTC on 26 September 2021. Moreover, the gaps in the assembling wind were almost not observed due to the usage of operational products from the four satellites in this study. The cyclonic structure of the storm is well represented. The maximum wind speed  $V_{max}$  reaches 45 m/s, which is greater than that shown in Figure 3 and is close to 46.26 m/s from NHC.

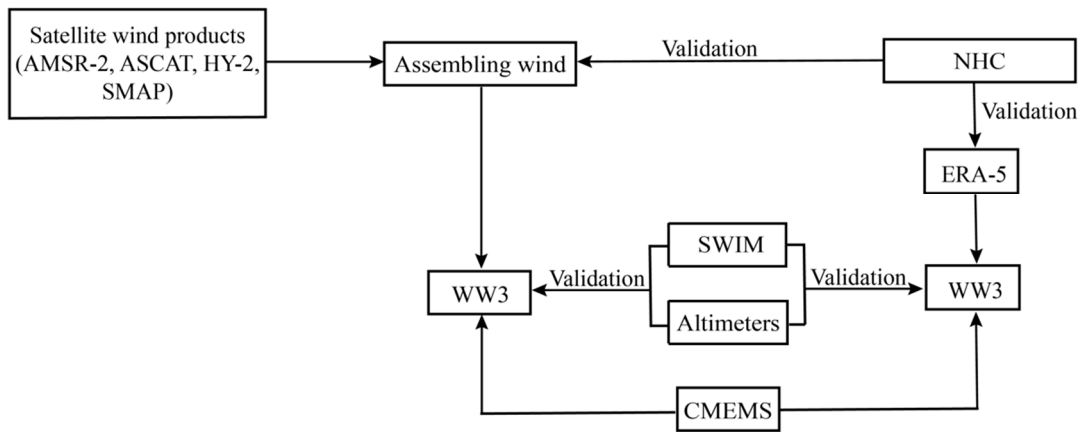


Figure 3. Diagrammatic sketch of this study.

### 2.2. Description and Settings of WW3

Both WW3 and SWAN are third-generation wave models (WAMs) [34] because they solve the wave equations of energy conservation. The balance equation in the direction of wave propagation is expressed as

$$\frac{\partial N}{\partial t} + \nabla \cdot [(c_g + c) \times N] = S_{in} + S_{bot} + S_{nl} + S_{other} \quad (3)$$

where  $N$  represents the wave action density spectrum;  $t$  is the time dimension;  $\nabla$  is the Hamiltonian operator interpreting the spatial dimension;  $c_g$  is the speed of the wave group;  $c$  is the background current speed;  $S_{in}$  is the input source produced by wind stress;  $S_{bot}$  is the wave–bottom interaction;  $S_{nl}$  represents non-linear triad and quadruplet wave–wave interactions; and  $S_{other}$  is the other sources, i.e., wave breaking and wave–current and wave–ice interactions. WW3 uses several parameterizations for these sources. In this study, the parametrization sets are selected according to previous studies, i.e., parametrizations of ST6+FLD2+BT1 for the input–dissipation source [16], parametrizations of TR1 for the source of wave–current interaction [14], and parametrizations of GMD2 for the source of wave–wave interactions [25]. The computational grid covers the region from 0° N to 60° N and from 100° E to 180° E, and the grid spacing is 0.1°.

The forcing fields include winds assembled using multiple remote-sensed products, currents, and sea levels. Here, the daily average sea surface current and sea level data from the Copernicus Marine Environment Monitoring Service (CMEMS) [35] are employed with 0.08° grid spacing. The water depth is based on the General Bathymetry Chart of the Oceans (GEBCOs) [36], with a horizontal resolution of 1 km. Other settings are listed as follows: frequency bin  $f$  is logarithmic, ranging from 0.04118 to 0.7186 at a 0.01 interval of  $\Delta f/f$ ; the directional resolution is 15°; and the time step is 300 s. The outputs from the WW3 model are SWH, peak wave period (PWP), and wave spectrum, with a spatial resolution of 0.1° at intervals of 1 h. In our work, the wave simulations of 30 typhoons continuously run with a ‘cold start’ regime from January 2021 to December 2022. As for the

‘cold start’ regime, several initial months of simulation results were used to establish the boundary conditions of the WW3 model. Thus, there is no prior information on the initial and boundary conditions for the wave spectrum simulation. In our study, we removed the initial 3 months simulation results to ensure the model accuracy of WW3.

### 2.3. ERA-5 Data

Since 1979, ECMWFs have continuously released atmospheric and marine data (i.e., wind and SWH) for the scientific community [37]. Until now, the spatial resolution of the latest ERA-5 wind and wave data has been 0.25° with a temporal resolution of 1 h, which is valuable for oceanographic research [38]. However, the ERA-5 wind and wave data during typhoons is significantly underestimated [39], although the TC size asymmetry in global climatology is reliable [40]. Figure 2d,e show the ERA-5 wind and SWH map during Typhoon Mindulle at 18:00 UTC on 26 September 2021, respectively. In this case, the maximum ERA-5 wind speed is 25 m/s, whereas the measurements from NHC are up to 46 m/s. The tropical cyclone reports of NHC contain the most accurate comprehensive information for each storm, including synoptic history, atmospheric statistics, casualties and damages, and the post-analysis best track. The NHC intensity (maximum 1 min average wind associated with the TC at an elevation of 10 m) from the best tracks is estimated using satellite-based techniques, i.e., the Advanced Microwave Sounding Unit and the multiplatform of satellites. Moreover, aircraft reconnaissance data and the Stepped Frequency Microwave Radiometer measurements are also used to reduce the NHC intensity uncertainty. In this study, ERA-5 data are employed to highlight the novelty of this study, i.e., the accuracy of assembling wind and wave parameters simulated by the WW3 model in typhoons because the ERA-5 data underestimate the wind speed under typhoon conditions. In other words, we applied the assembling wind rather than the ERA-5 wind data as the forcing field to improve the accuracy of the wave simulations from the WW3 model.

### 2.4. Metric Parameters

Two parameters, root-mean-squared error (RMSE) and scatter index (SI) [41,42], are employed for the error analysis of the variables, i.e., the maximum wind speed  $V_{max}$ , SWH, and PWP:

$$RMSE = \sqrt{\frac{1}{n} \sum_{i=1}^n (X_i - Y_i)^2} \tag{4}$$

$$SI = \frac{1}{\bar{Y}} \sqrt{\frac{\sum_{i=1}^n \left[ \left( X_i - \bar{X} \right) - \left( Y_i - \bar{Y} \right) \right]^2}{n}} \tag{5}$$

where the  $n$ -elements  $X_i$  and  $Y_i$  represent the modeled and measured data. The correlation coefficient (Cor) and the squared error (Err) are defined as

$$Cor = \frac{\sum P_k Q_k \Delta k}{\sqrt{\sum P_k^2 Q_k^2 \Delta k}} \tag{6}$$

$$Err = \frac{2 \Delta f}{\sqrt{\sum P_f^2 \Delta f \sum Q_f^2 \Delta f}} \tag{7}$$

where  $P_f$  and  $Q_f$  represent the one-dimensional wave spectrum in terms of wave frequency  $f$  simulated by the WW3 model and measured by SWIM, respectively.

A diagrammatic sketch of this study is shown in Figure 3.

## 3. Results

In this section, the applicability of assembling winds during storms is assessed, and the validation of WW3-simulated waves against the products of SWIM is discussed. Fur-

thermore, a comparison between the WW3 result forced by assembling wind and ERA-5 wind is presented.

### 3.1. Applicability of Assembling Winds

The comparison between the maximum wind speed ( $V_{max}$ ) in 30 typhoons and the measurements from NHC was statistically analyzed, yielding an RMSE of 4.79 m/s and an SI of 0.20 for the assembling wind and an RMSE of 9.20 m/s and an SI of 0.37 for the ERA-5, as exhibited in Figure 4a. Similarly, the comparison between the assembling wind and ERA-5 data in the 30-typhoon period is depicted in Figure 4b. It is found that the underestimation in the results from the ERA-5 data is reduced in a typhoon period. In addition, the assembling wind speeds are close to that of ERA-5 under low-to-moderate atmospheric conditions.

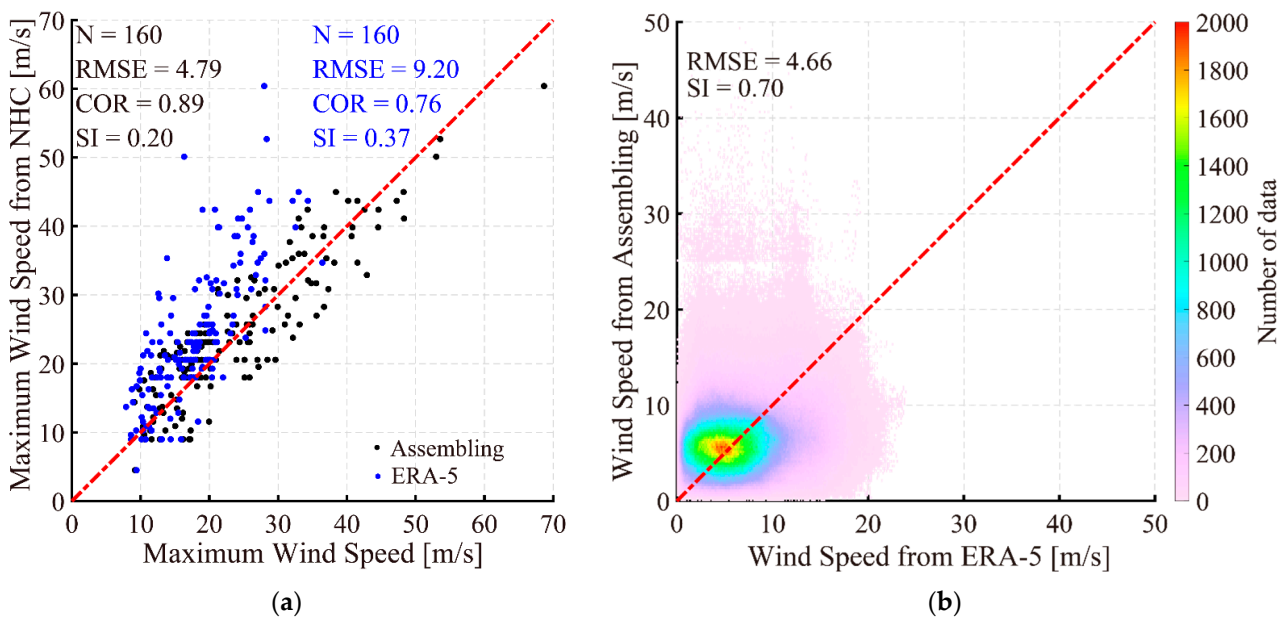


**Figure 4.** (a) Comparison of the maximum wind speed  $V_{max}$  between assembling data, ERA-5 data, and the measurements from NHC in 30 typhoons. (b) Comparison between assembling wind and ERA-5 data from 30 typhoons.

### 3.2. Validation of WW3-Simulated Waves

It was proven in previous studies [3,13,14] that WW3 has good performances in hindcasting typhoon-induced waves over many parts of the global ocean. Assembling wind, CEMES currents, and CMEMS sea levels are treated as forcing in WW3 (version 6.07). In our study, the WW3-simulated waves for June–October 2022 are validated against the measurements from SWIM onboard CFOSAT and measurements observed from altimeter Jason-3. The WW3-simulated SWHs map during Typhoon Mindulle at 00:00 UTC on 26 September 2021 is shown in Figure 5a,c, in which the along-track SWHs from SWIM and Jason-3 are also shown. As shown in Figure 5d, there are over 500,000 matchups between the WW3 simulations and the measurements from altimeter Jason-3, with a 0.44 m RMSE, 0.28 SI, and a 0.83 Cor. The variation in SWH via the ERA-5 wave, the utilized approach, WW3 forced by ERA-5 wind, and the footprint of SWIM is illustrated in Figure 5b. The variation in SWH via assembling winds from WW3 and the footprint of SWIM is consistent at SWH up to 8 m. Furthermore, the wave simulations using assembling wind products are better than those in ERA-5 and the SWH via the WW3 model forced by ERA-5 wind, with an improvement of up to about 1 m. Additionally, the time difference between WW3 and SWIM is less than 30 min. Statistical analysis was conducted for 30 typhoons, yielding a 0.80 Cor of wave spectrum with a 0.49 Err, a 0.48 m RMSE of SWH with a 0.25 SI (Figure 6a), and a 0.95 s RMSE of PWP with a 0.1 SI (Figure 6b). Under this circumstance, it

is believed that assembling wind derived from multiple remote-sensed products is reliable for typhoon-induced wave simulation via WW3.

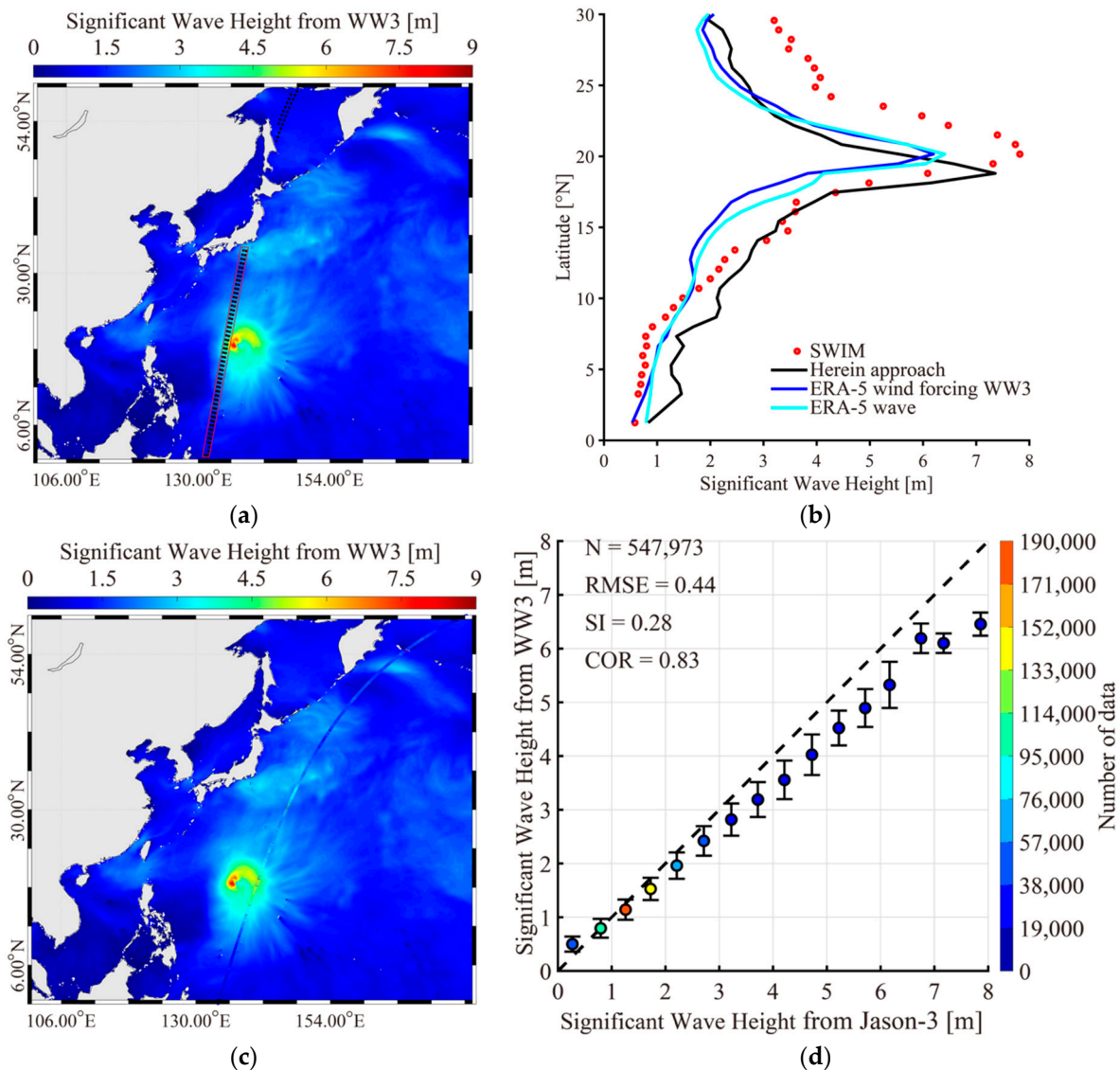


**Figure 5.** (a) Distributions of SWHs from WAVEWATCH-III (WW3), in which along-track SWHs were measured via SWIM onboard CFOSAT. (b) Along-track variation in SWHs from ERA-5, WW3, and the footprint of SWIM. (c) SWH map from WAVEWATCH-III (WW3), in which along-track SWHs were measured using the Jason-3 altimeter. (d) SWH comparison between WW3 and measurements from the Jason-3 altimeter.

As mentioned in Section 2, ERA-5 provides wave data over the global ocean, especially in TCs. Therefore, the bias of SWH (WW3-simulated SWH minus ERA-5) relative to the bias of wind (assembling minus ERA-5) was analyzed, as exhibited in Figure 7. It is not surprising that a positive bias occurs as the bias of wind speeds is larger than 5 m/s, which means that the bias of SWH has a positive relation with the bias of wind speed. This is because the sea surface wave is mainly determined by wind stress [13]. Moreover, the bias of SWH increases with the increasing bias of wind speed. In particular, the bias of SWHs could reach 4 m as the wind speed bias is greater than 30 m/s. Therefore, the assembling wind from multiple scatterometers and radiometers is a promising source of data for wave simulation via the WW3 model during typhoons because the underestimation of strong wind from the atmospheric model (i.e., ERA-5) is improved.

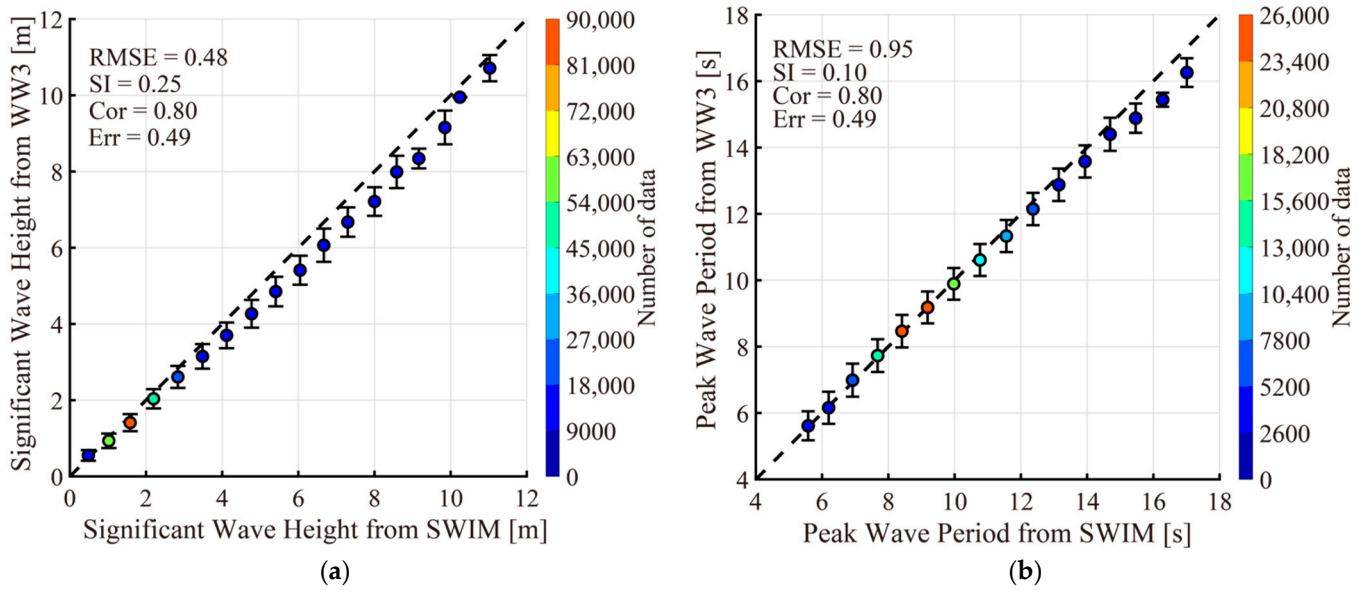


**Figure 6.** (a) Comparison of SWHs between WW3 and SWIM. (b) Comparison of peak wave period (PWP) between WW3 and SWIM.

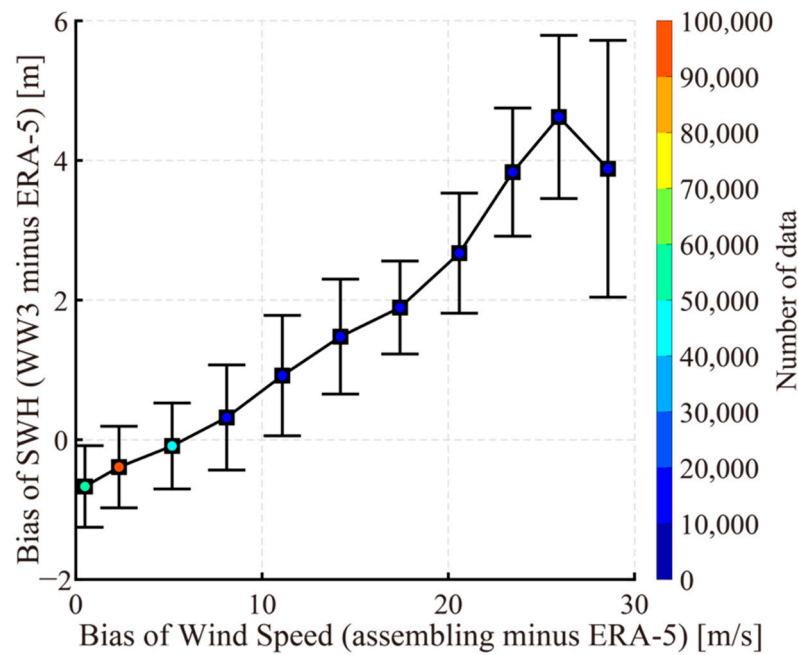


**Figure 7.** Bias (WW3-simulated SWH minus ERA-5) versus assembling wind speed.

### 3.3. Discussion

The ERA-5 winds and assembling winds were used as the forcing field for the WW3 model, and we compared the wave parameters from July to October 2021. Figure 8 shows the comparison between the SWH simulated via the WW3 model with the ERA-5 wind forcing, and the assembling wind forcing and the measurements from SWIM. Statistical analysis was conducted, yielding a Cor of 0.91, with an RMSE of SWH of 0.41m simulated via the WW3 model with the assembling wind forcing and an SI of 0.20 (Figure 8a), which is better than the SWH simulated via the WW3 model with the ERA-5 wind forcing shown in Figure 8b with a Cor of 0.86, an RMSE of 0.49 m, and an SI of 0.27. In addition, the Cor of the PWP simulated via the WW3 model with the assembling wind forcing was 0.69, with an RMSE of 1.23 m and an SI of 0.13 (Figure 8c). The result is better than the PWP simulated via the WW3 model with the ERA-5 winds forcing, as exhibited in Figure 8d.

Furthermore, Figure 9 shows a variation in the SWH relative to the measurements from SWIM, in which the red error bar represents the bias of SWHs (simulations from the WW3 model with the assembling wind forcing minus the measurements from SWIM), and the black error bar is the bias of SWHs (simulations from the WW3 model with the ERA-5 wind forcing minus the measurements from SWIM). It was found that the bias of SWHs simulated via assembling forcing winds was less than that via ERA-5 forcing winds. With the increase in the SWIM-measured SWHs, the bias increased. However, the bias of SWHs simulated via assembling forcing winds was significantly smaller than that via ERA-5 forcing winds at SWH > 3 m, and this behavior was even more obvious at the extreme sea state. Under this circumstance, it is believed that assembling winds derived from multiple remote-sensed products is better for typhoon-induced wave simulation using the WW3 model than using ERA-5 winds.

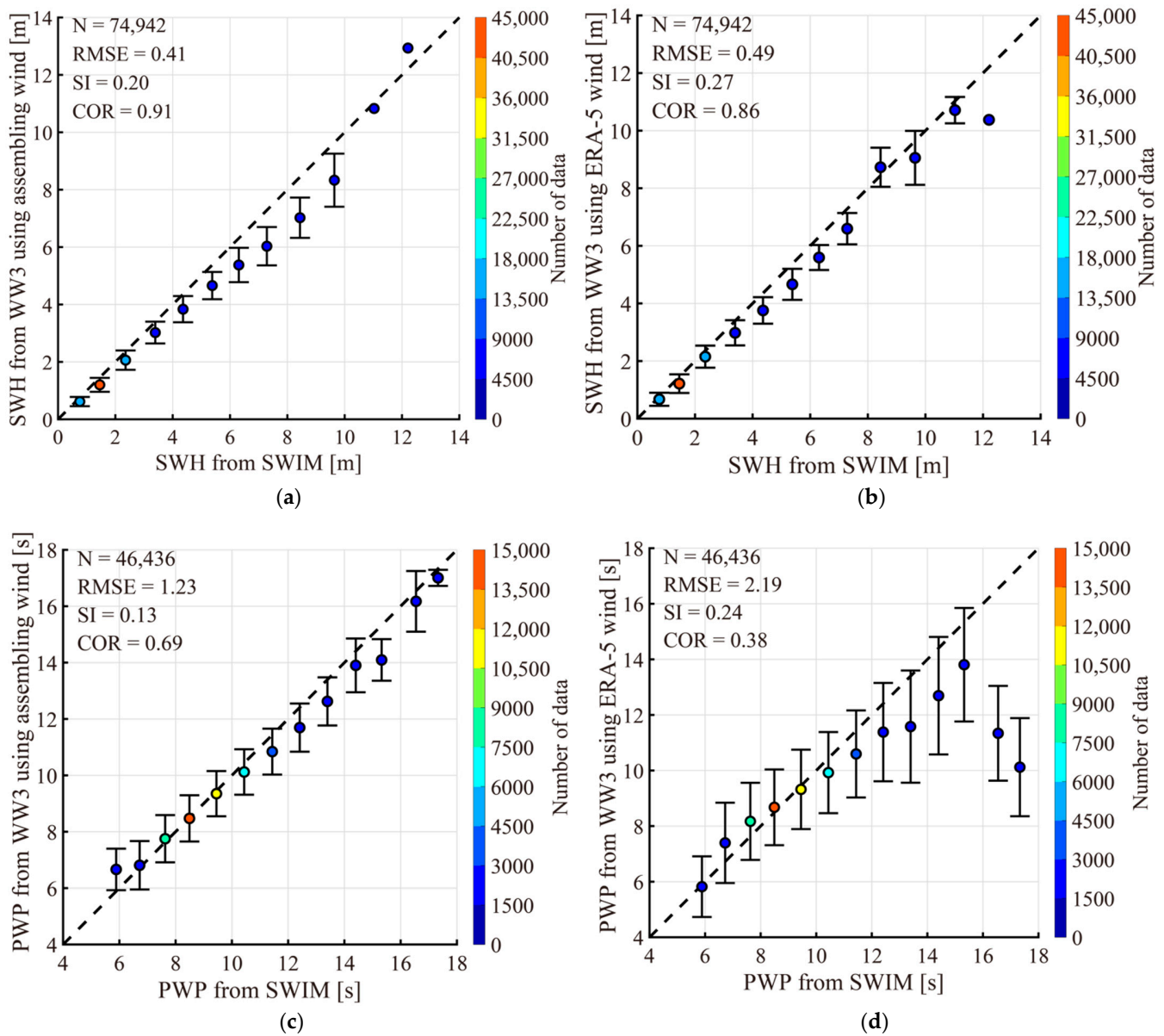


**Figure 8.** (a) SWH comparison between WW3 model with the assembling wind forcing and SWIM. (b) SWH comparison between WW3 model with the ERA-5 wind forcing and SWIM. (c) Comparison of peak wave period (PWP) between WW3 model with the assembling wind forcing and SWIM. (d) Comparison of peak wave period (PWP) between WW3 model with the ERA-5 wind forcing and SWIM.

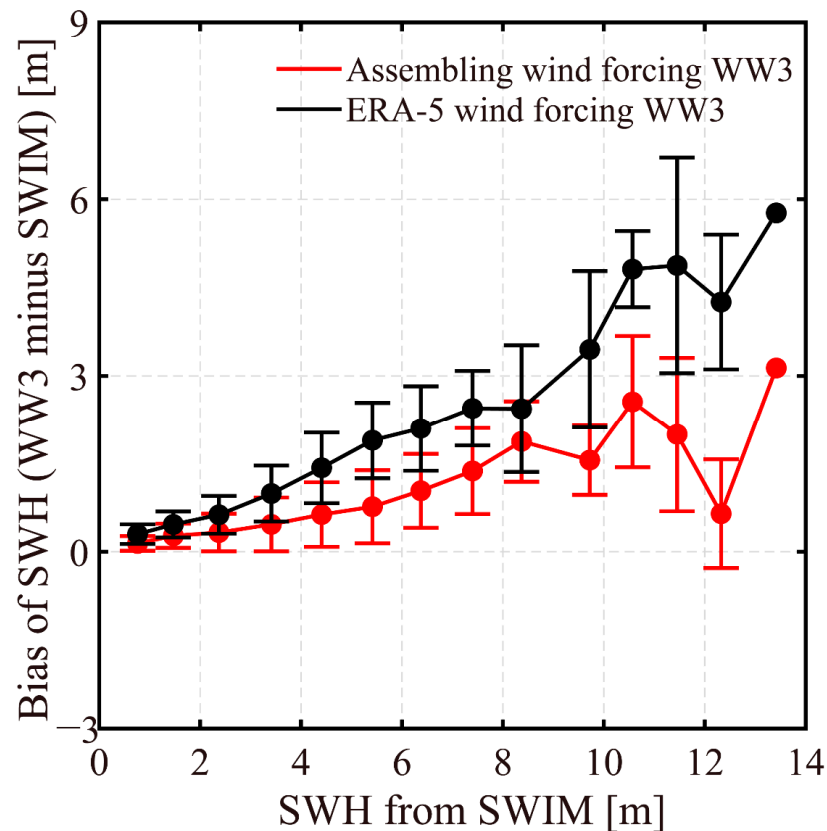


**Figure 9.** Bias of SWH versus the measurement of SWIM SWH, in which the red error bar represents the bias of SWH (simulated from the WW3 model with the assembling wind forcing minus that measured by SWIM), and the black error bar is the bias of SWH (simulated from the WW3 model with the ERA-5 wind forcing minus that measured by SWIM).

#### 4. Conclusions

Remote-sensed wind and wave products are operationally provided by multiple satellites, i.e., ASCAT [43], HY-2B [44], and CFOSAT [45]. Although the spatial resolution of these products is 12.5 km for winds and  $\sim 10$  km for waves, they are valuable sources of data for oceanography during extreme sea states [46], e.g., typhoons and hurricanes. As mentioned above, the wind field simulated using atmospheric models such as ERA-5 during typhoons is significantly underestimated. The purpose of this study is to address the issue of whether assembling winds from satellites is valuable as a forcing field in wave simulation via the WW3 model. Although the advantage of the proposed approach is that TC intensity is considerable, the uncertainty of remote-sensed products is inherent in assembling winds.

In our study, wind products from the scatterometers and radiometers during the typhoon season in 2021 and 2022 were assembled using the Cressman interpolation method. The statistical analysis of the maximum wind speed  $V_{max}$  in 30 typhoons from assembling winds compared with the measurements from NHC showed an RMSE of 4.79 m/s and an SI of 0.20. In addition, the comparison between assembling wind speeds and ERA-5 data proved that underestimation exists in the result from the numerical weather prediction model. This indicates that assembling winds could illustrate the intensity of the typhoon. The  $0.125^\circ$  gridded assembling wind speeds with intervals of 12 h, daily CMEMS currents, and daily CMEMS sea levels at  $0.08^\circ$  grids which were applied as the forcing fields in the WW3 wave simulations during 30 typhoons. The WW3-simulated waves for June–October 2022 were validated against the measurements from SWIM onboard CFOSAT, yielding a Cor of wave spectrum of 0.80 with an Err of 0.49, an RMSE of SWHs of 0.48 m with an SI of 0.25, and an RMSE of PWP of 0.95 s with an SI of 0.10. Furthermore, an error

analysis between the bias of SWHs (WW3 minus ERA-5) concerning the bias of wind speeds (assembling minus ERA-5) was conducted. It was observed that the WW3-simulated SWHs forced by the assembling wind fields was higher than that by ERA-5, i.e., the positive bias of SWHs at a wind speed bias greater than 5 m/s. With the increasing bias of wind speeds, the bias of SWHs gradually increased; in particular, the bias of SWHs reached up to 4 m as the wind speed bias was greater than 30 m/s, which was caused by the linear relation between winds and waves. Furthermore, the comparison also showed that assembling winds derived from multiple remote-sensed products had better performance for typhoon-induced wave simulations using WW3 than that using the ERA-5 winds. In particular, the error reduced from 6 m with ERA-5 winds to 3 m with assembling winds in an extreme sea state. It was concluded that assembling winds derived from multiple remote-sensed products is reliable for typhoon-induced wave simulations using WW3, in which the underestimation of ERA-5 in typhoons is significantly reduced.

TC winds and waves can be inverted from SAR images with fine spatial resolution, i.e., TerraSAR-X [47,48], Gaofen-3 [49], RADARSAT-2 [50], and Sentinel-1 [51,52]. In the near future, SAR-derived TC winds and waves will be assimilated with other remote-sensed wind products. Otherwise, by assembling winds using the interpolation method, we need to consider the asymmetric of the typhoon winds [53]. The collocated wind and wave data are useful for improving the parametrizations of the drag coefficient and wave breaking in WW3 to enhance the accuracy of the wave simulation.

**Author Contributions:** Conceptualization, W.S. and R.Y.; methodology, W.S. and M.W.; validation, W.S. and Y.Z.; formal analysis, W.S., M.W. and R.Y.; investigation, W.S. and J.Z.; resources, W.S.; writing—original draft preparation, W.S. and R.Y.; writing—review and editing, J.Z. and S.H.; visualization, R.Y., M.W. and J.Z.; funding acquisition, W.S. and J.Z. All authors have read and agreed to the published version of the manuscript.

**Funding:** This research was funded by the National Natural Science Foundation of China under Contract No. 42076238, 42176012, and 42130402 and the Natural Science Foundation of Shanghai under Contract No. 23ZR1426900.

**Institutional Review Board Statement:** Not applicable.

**Informed Consent Statement:** Not applicable.

**Data Availability Statement:** Due to the nature of this research, the participants of this study did not agree to their data being shared publicly, so supporting data are not available.

**Acknowledgments:** We truly appreciate the provision of WAVEWATCH-III (WW3) by the National Centers for Environmental Prediction (NCEP) of the National Oceanic and Atmospheric Administration (NOAA). The information on typhoons was collected from the National Hurricane Center (NHC). Advanced Scatterometer (ASCAT) wind data were downloaded from <http://archive.eumetsat.int> (accessed on 9 October 2023) using an authorized account. The wind data from Haiyang-2 (HY-2) and wave data from Surface Waves Investigation and Monitoring (SWIM) were provided by the National Satellite Ocean Application Service (NSOAS) through an authorized account via <https://osdds.nsoas.org.cn> (accessed on 9 October 2023). Operational wind products from Soil Moisture Active–Passive (SMAP) radiometer and Advanced Microwave Scanning Radiometer-2 (AMSR-2), generated via remote sensing systems, were obtained from <http://www.remss.com> (accessed on 9 October 2023). The daily average sea surface current and sea level data from the Copernicus Marine Environment Monitoring Service (CMEMS) were accessed via <https://marine.copernicus.eu> (accessed on 9 October 2023). The bathymetric topography from the General Bathymetry Chart of the Oceans (GEBCOs) can be accessed via <ftp.edcftp.cr.usgs.gov> (accessed on 9 October 2023).

**Conflicts of Interest:** The authors declare no conflict of interest.

## References

1. Wang, H.J.; Sun, J.Q.; Fan, K. Relationships between the North Pacific Oscillation and the typhoon/hurricane frequencies. *Sci. China Ser. D* **2007**, *50*, 1409–1416. [[CrossRef](#)]
2. Vogelzang, J.; Stoffelen, A. ASCAT ultrahigh-resolution wind products on optimized grids. *IEEE J. Sel. Topics Appl. Earth Observ. Remote Sens.* **2017**, *10*, 2332–2339. [[CrossRef](#)]

3. Wang, H.; Mouche, A.; Husson, R.; Chapron, B.; Yang, J.S.; Liu, J.Q.; Ren, L. Quantifying uncertainties in the partitioned swell heights observed from CFOSAT SWIM and Sentinel-1 SAR via triple collocation. *IEEE Trans. Geosci. Remote Sens.* **2022**, *60*, 4207716. [[CrossRef](#)]
4. Kudryavtsev, V.N.; Chapron, B.; Myasoedov, A.G.; Collard, F.; Johannessen, J.A. On dual co-polarized SAR measurements of the ocean surface. *IEEE Geosci. Remote Sens. Lett.* **2013**, *10*, 761–765. [[CrossRef](#)]
5. Shao, W.Z.; Hu, Y.Y.; Jiang, X.W.; Zhang, Y.G. Wave retrieval from quad-polarized Chinese Gaofen-3 SAR image using an improved tilt modulation transfer function. *Geo-Spat. Inf. Sci.* **2023**, 1–19. [[CrossRef](#)]
6. Vickery, P.J.; Masters, F.J.; Powell, M.D.; Wadhera, D. Hurricane hazard modeling: The past, present, and future. *J. Wind Eng. Ind. Aerod.* **2009**, *97*, 392–405. [[CrossRef](#)]
7. Wang, Z.F.; Gong, Y.J.; Cui, J.N.; Dong, S.; Wu, K.J. Effect of the drag coefficient on a typhoon wave model. *J. Oceanol. Limn.* **2019**, *37*, 1795–1804. [[CrossRef](#)]
8. Zijlema, M.; Westhuysen, A. On convergence behavior and numerical accuracy in stationary SWAN simulations of nearshore wind wave spectra. *Coast Eng.* **2005**, *52*, 237–256. [[CrossRef](#)]
9. Zhang, C.; Hou, Y.J.; Li, J. Wave-current interaction during Typhoon Nuri (2008) and Hagupit (2008): An application of the coupled ocean-wave modeling system in the northern South China Sea. *J. Oceanol. Limn.* **2018**, *36*, 65–77. [[CrossRef](#)]
10. Sun, M.H.; Duan, Y.H.; Zhu, J.R.; Wu, H.; Zhang, J.; Huang, W. Simulation of Typhoon Muifa using a mesoscale coupled atmosphere-ocean model. *Acta Oceanol. Sin.* **2014**, *33*, 123–133. [[CrossRef](#)]
11. Li, X.H.; Yang, J.S.; Han, G.Q.; Ren, L.; Zheng, G.; Chen, P.; Zhang, H. Tropical cyclone wind field reconstruction and validation using measurements from SFMR and SMAP radiometer. *Remote Sens.* **2022**, *14*, 3929. [[CrossRef](#)]
12. Hersbach, H. Comparison of C-Band Scatterometer CMOD5.N equivalent neutral winds with ECMWF. *J. Atmos. Ocean. Technol.* **2010**, *27*, 721–736. [[CrossRef](#)]
13. Brus, S.R.; Wolfram, P.J.; Van Roekel, L.P.; Meixner, J.D. Unstructured global to coastal wave modeling for the Energy Exascale Earth System Model using WAVEWATCH III version 6.07. *Geosci. Model Dev.* **2021**, *14*, 2917–2938. [[CrossRef](#)]
14. Wang, J.C.; Zhang, J.; Yang, J.G. Numerical simulation and preliminary analysis on ocean waves during Typhoon Nesat in South China Sea and adjacent areas. *Chin. J. Oceanol. Limnol.* **2014**, *32*, 665–680. [[CrossRef](#)]
15. The WAVEWATCH III Development Group (WW3DG). *User Manual and System Documentation of WAVEWATCH III*; Version 5.16; Tech. Note 329; NOAA/NWS/NCEP/MMAB: College Park, MD, USA, 2016; Volume 276, p. 326.
16. Shao, W.Z.; Yu, W.P.; Jiang, X.W.; Shi, J.; Wei, Y.L.; Ji, Q.Y. Analysis of wave distributions using the WAVEWATCH-III model in the Arctic Ocean. *J. Ocean Univ. China* **2022**, *21*, 15–21. [[CrossRef](#)]
17. Rogers, W.E.; Hwang, P.A.; Wang, D.W. Investigation of wave growth and decay in the SWAN model: Three regional-scale applications. *J. Phys. Oceanogr.* **2010**, *33*, 366–389. [[CrossRef](#)]
18. Chen, Y.R.; Chen, L.H.; Zhang, H.; Gong, W.P. Effects of wave-current interaction on the Pearl River Estuary during Typhoon Hato. *Estuar. Coast. Shelf Sci.* **2019**, *228*, 106364. [[CrossRef](#)]
19. Amrutha, M.M.; Kumar, V.S.; Sandhya, K.G.; Nair, T.M.B.; Rathod, J.L. Wave hindcast studies using SWAN nested in WAVEWATCH III-comparison with measured nearshore buoy data off Karwar, eastern Arabian Sea. *Ocean Eng.* **2016**, *119*, 114–124. [[CrossRef](#)]
20. Liu, Q.X.; Alexander, V.B.; Stefan, Z.; Young, L.R.; Guan, C.L. Wind and wave climate in the Arctic Ocean as observed by Altimeters. *J. Clim.* **2016**, *29*, 7957–7975. [[CrossRef](#)]
21. Li, J.D.; Babanin, A.V.; Liu, Q.X.; Voermans, J.J.; Heil, P.; Tang, Y.M. Effects of wave-induced sea ice break-up and mixing in a high-resolution coupled ice-ocean model. *J. Mar. Sci. Eng.* **2021**, *9*, 365. [[CrossRef](#)]
22. Akpınar, A.; van Vledder, G.P.; Kömürcü, M.İ.; Özger, M. Evaluation of the numerical wave model (SWAN) for wave simulation in the Black Sea. *Cont. Shelf Res.* **2012**, *50*, 80–99. [[CrossRef](#)]
23. Holland, G.J. An analytic model of the wind and pressure profiles in hurricanes. *Mon. Weather Rev.* **1980**, *108*, 1212–1218. [[CrossRef](#)]
24. Shi, J.; Shao, W.Z.; Shi, S.S.; Hu, Y.Y.; Jiang, T.; Zhang, Y.G. Can sea surface waves be simulated by numerical wave models using the fusion data from remote-sensed winds? *Remote Sens.* **2023**, *15*, 3825. [[CrossRef](#)]
25. Hu, Y.Y.; Shao, W.Z.; Shen, W.; Zuo, J.C.; Jiang, T.; Hu, S. Analysis of sea surface temperature cooling in typhoon events passing the Kuroshio current. *J. Ocean Univ. China* **2023**. [[CrossRef](#)]
26. Jin, Q.; Fan, X.; Liu, J.; Xue, Z.; Jian, H. Estimating tropical cyclone intensity in the South China sea using the XGBoost model and Fengyun satellite images. *Atmosphere* **2020**, *11*, 423. [[CrossRef](#)]
27. Gao, Y.; Guan, C.L.; Sun, J.; Xie, L. Tropical cyclone wind speed retrieval from dual-polarization Sentinel-1 EW mode products. *J. Atmos. Ocean. Technol.* **2020**, *3*, 1713–1724. [[CrossRef](#)]
28. Park, M.S.; Kim, M.; Lee, M.I.; Im, J.; Park, S. Detection of tropical cyclone genesis via quantitative satellite ocean surface wind pattern and intensity analyses using decision trees. *Remote Sens. Environ.* **2016**, *183*, 205–214. [[CrossRef](#)]
29. Shao, W.Z.; Jiang, T.; Jiang, X.W.; Zhang, Y.G.; Zhou, W. Evaluation of sea surface winds and waves retrieved from the Chinese HY-2B data. *IEEE J. Sel. Topics Appl. Earth Observ. Remote Sens.* **2021**, *14*, 9624–9635. [[CrossRef](#)]
30. Zhang, B.; Li, X.F.; Perrie, W.; He, Y.J. Synergistic measurements of ocean winds and waves from SAR. *J. Geophys. Res. Oceans* **2015**, *120*, 6164–6184. [[CrossRef](#)]

31. Wang, X.C.; Han, B.; Zhong, L.H.; Yuan, X.Z. Retrieval of significant wave height under typhoon conditions from Gaofen-3 SAR imagery. *J. Ocean U. China* **2022**, *21*, 81–90. [\[CrossRef\]](#)
32. Hao, M.; Shao, W.; Shi, S.; Liu, X.; Hu, Y.; Zuo, J. Validation of Surface Waves Investigation and Monitoring Data against Simulation by Simulating Waves Nearshore and wave retrieval from Gaofen-3 synthetic aperture radar image. *Remote Sens.* **2023**, *15*, 4402. [\[CrossRef\]](#)
33. Sun, H.Y.; Geng, X.P.; Meng, L.S.; Yan, X.H. First ocean wave retrieval from HISEA-1 SAR Imagery through an improved semi-automatic empirical model. *Remote Sens.* **2023**, *15*, 3486. [\[CrossRef\]](#)
34. Tolman, H.L.; Chalikov, D.V. Source terms in a third-generation wind wave model. *J. Phys. Oceanogr.* **1996**, *26*, 2497–2518. [\[CrossRef\]](#)
35. Zhang, X.; Cheng, L.; Zhang, F.; Wu, J.; Ki, M. Evaluation of multi-source forcing datasets for drift trajectory prediction using Lagrangian models in the South China Sea. *Appl. Ocean Res.* **2020**, *104*, 102395. [\[CrossRef\]](#)
36. Kapoor, D.C. General bathymetric chart of the oceans (GEBCO). *Mar. Geod.* **1981**, *5*, 73–80. [\[CrossRef\]](#)
37. Molteni, F.; Buizza, R.; Palmer, T.N.; Petroliagis, T. The ECMWF ensemble prediction system: Methodology and validation. *Q. J. Roy. Meteor. Soc.* **1996**, *122*, 73–119. [\[CrossRef\]](#)
38. Takbash, A.; Young, I.R. Long-term and seasonal trends in global wave height extremes derived from ERA-5 reanalysis data. *J. Mar. Sci. Eng.* **2020**, *8*, 1015. [\[CrossRef\]](#)
39. Han, Z.H.; Yue, C.J.; Liu, C.; Gu, W.; Tang, T.Q.; Li, Y.J. Evaluation on the applicability of ERA5 reanalysis dataset to tropical cyclones affecting Shanghai. *Front. Earth Sci.* **2022**, *16*, 1025–1039. [\[CrossRef\]](#)
40. Zhang, K.L.; Chan, K.T. An ERA5 global climatology of tropical cyclone size asymmetry. *Int. J. Climatol.* **2023**, *43*, 950–963. [\[CrossRef\]](#)
41. Shao, W.Z.; Jiang, X.W.; Sun, Z.F.; Hu, Y.Y.; Marino, A.; Zhang, Y.G. Evaluation of wave retrieval for Chinese Gaofen-3 synthetic aperture radar. *Geo-Spat. Inf. Sci.* **2022**, *25*, 229–243. [\[CrossRef\]](#)
42. Bhattacharya, D.; Sinha, N. Scatter Index: An alternative measure of dispersion based on relative frequency of occurrence of observations. In *Data Engineering and Intelligent Computing*; Springer: Singapore, 2022; Volume 446. [\[CrossRef\]](#)
43. Figa-Saldaña, J.; Wilson, J.W.; Attema, E.; Gelsthorpe, R.; Drinkwater, M.R.; Stoffelen, A. The advanced scatterometer (ASCAT) on the meteorological operational (MetOp) platform: A follow on for European wind scatterometers. *Can. J. Remote Sens.* **2002**, *28*, 404–412. [\[CrossRef\]](#)
44. Yang, S.; Mu, B.; Shi, H.; Ma, C.; Zhou, W.; Zou, J.; Lin, M. Validation and accuracy analysis of wind products from scatterometer onboard the HY-2B satellite. *Acta Oceanol. Sin.* **2023**, *42*, 74–82. [\[CrossRef\]](#)
45. Dong, X.L.; Zhu, D.; Lin, W.M.; Liu, H.G.; Jiang, J.S. Status and recent progresses of development of the scatterometer of CFOSAT. In Proceedings of the 2011 IEEE International Geoscience and Remote Sensing Symposium, Vancouver, BC, Canada, 24–29 July 2011; pp. 961–964.
46. Permyakov, M.; Kleshcheva, T.; Potalova, E.; Holzworth, R.H. Characteristics of typhoon eyewalls according to world wide lightning location network data. *Mon. Weather Rev.* **2019**, *147*, 4027–4043. [\[CrossRef\]](#)
47. Corcione, V.; Grieco, G.; Portabella, M.; Nunziata, F.; Migliaccio, M. A novel azimuth cutoff implementation to retrieve sea surface wind speed from SAR imagery. *IEEE Trans. Geosci. Remote Sens.* **2019**, *57*, 3331–3340. [\[CrossRef\]](#)
48. Corcione, V.; Nunziata, F.; Migliaccio, M. Megi typhoon monitoring by X-Band Synthetic Aperture Radar measurements. *IEEE J. Oceanic Eng.* **2018**, *43*, 184–194. [\[CrossRef\]](#)
49. Wang, H.; Yang, J.; Lin, M.; Li, W.; Zhu, J.; Ren, L.; Cui, L. Quad-polarimetric SAR sea state retrieval algorithm from Chinese Gaofen-3 wave mode images via deep learning. *Remote Sens. Environ.* **2022**, *273*, 112969. [\[CrossRef\]](#)
50. Zhang, G.S.; Li, X.F.; Perrie, W.; Hwang, P.; Zhang, B.; Yang, X.F. A hurricane wind speed retrieval model for C-band RADARSAT-2 cross-polarization ScanSAR images. *IEEE Trans. Geosci. Remote Sens.* **2017**, *55*, 4766–4774. [\[CrossRef\]](#)
51. Mouche, A.; Chapron, B.; Knaff, J.; Zhao, Y.; Zhang, B.; Combot, C. Copolarized and cross-polarized sar measurements for high-resolution description of major hurricane wind structures: Application to irma category 5 hurricane. *J. Geophys. Res.-Oceans.* **2019**, *124*, 3905–3922. [\[CrossRef\]](#)
52. Zhang, L.; Liu, G.Q.; Perrie, W.; He, Y.J.; Zhang, G.S. Typhoon/Hurricane-generated wind waves inferred from SAR imagery. *Remote Sens.* **2018**, *10*, 1605. [\[CrossRef\]](#)
53. Wang, P.C.; Sheng, J.Y. A comparative study of wave-current interactions over the eastern Canadian shelf under severe weather conditions using a coupled wave-circulation model. *J. Geophys. Res. Oceans* **2016**, *121*, 5252–5281. [\[CrossRef\]](#)

**Disclaimer/Publisher’s Note:** The statements, opinions and data contained in all publications are solely those of the individual author(s) and contributor(s) and not of MDPI and/or the editor(s). MDPI and/or the editor(s) disclaim responsibility for any injury to people or property resulting from any ideas, methods, instructions or products referred to in the content.